
Supporting Information

Magnetic Pillar Induced Poiseuille-like Flow in Microfluidic Channels with Viscous and Viscoelastic Fluids

Charles Paul Moore^{1,2*}, Stefan Rouach², Marine Le Goas², Sandra Lerouge², Nicolas Tsapis³, Jérôme Fresnais¹ and Jean-François Berret^{2*}

¹*Sorbonne Université, CNRS, Laboratoire de Physicochimie des Electrolytes et Nanosystèmes Interfaciaux, PHENIX, UMR8234, F-75252 Paris Cedex 05, France*

²*Université Paris Cité, CNRS, Matière et systèmes complexes, 75013 Paris, France*

³*Université Paris-Saclay, CNRS, Institut Galien Paris-Saclay, 91400 Orsay, France*

Outline

S1 – Size distribution of the iron carbonyl microparticles

S2 – Elemental maps and fractions of carbon, silicon, iron and oxygen obtained from energy-dispersive X-ray (EDX) analysis

S3 – Iron carbonyl microparticle (FeMPs) powder magnetization curve

S4 – Wide-Angle X-Ray Scattering (WAXS) on FeMP iron microparticles

S5 - Comparison of pillar motion along the x - and y -direction

S6 – Bead motion shows pulsatile pattern as a function of time

S7 – Image of magnetic micropillar arrays in binocular microscopy

S8 - Magnetic field measurements under translational motion: experiments and simulations

S9 - Detailed simulation procedure

Additional supporting information

Original avi-file: “Movie#1_Micropillars_translatioActuation.avi”

Sequence of optical microscopy images showing a pillar substrate under the application of a magnetic field. The experimental conditions are: Pillar height = 70 μm , diameter = 18 μm - Materials: PDMS with 10 vol. % of iron particles - Asymmetric sawtooth wave applied by a micromanipulator holding the magnet

Original avi-file: “Movie#2_MicropillarActuation.avi”

Movie showing the actuation of 4 micropillars at a rate of 5.6 Hz (top panel). The position of the leftmost micropillar tip is shown in both the horizontal (x) and vertical (y) directions (bottom panel). Original movie taken at a rate of 240 frames/s, and current version has a duration of 14 sec.

Original avi-file: “Movie#3_ReversibleFlowByMicropillars.avi”

Movie showing in the first panel (left) the actuation of micropillars. The corresponding flow in the view field of the microchannel is shown (middle). A highlighted suspended microbead, and it

is displacement over time are shown (right). The microchannel in question is filled with a 1% micellar solution, with microbeads suspended. Micropillars are actuated at a rate of 5.6 Hz. Original movies are taken at 30 fps, and current version has a duration of 14 sec.

Original avi-file: “Movie#4_PulsatileFlow.avi”

Movie showing the motion of microbeads suspended in water, being actuated by micropillars at 5.6 Hz. A single suspended microbead is highlighted, and its position is shown with respect time tome. The original movie is taken at 240 fps, and the current version has a duration of 8 sec.

Keywords:

magnetic artificial cilia | flow generation | magnetic particles | stimuli responsive substrates | low Reynolds number | mucociliary clearance

Corresponding authors: paul.moore@u-paris.fr; jean-francois.berret@u-paris.fr

This version Tuesday, April 29, 25

To be submitted to Lab on Chip

Supporting Information S1

Size distribution of the iron carbonyl microparticles (FeMPs)

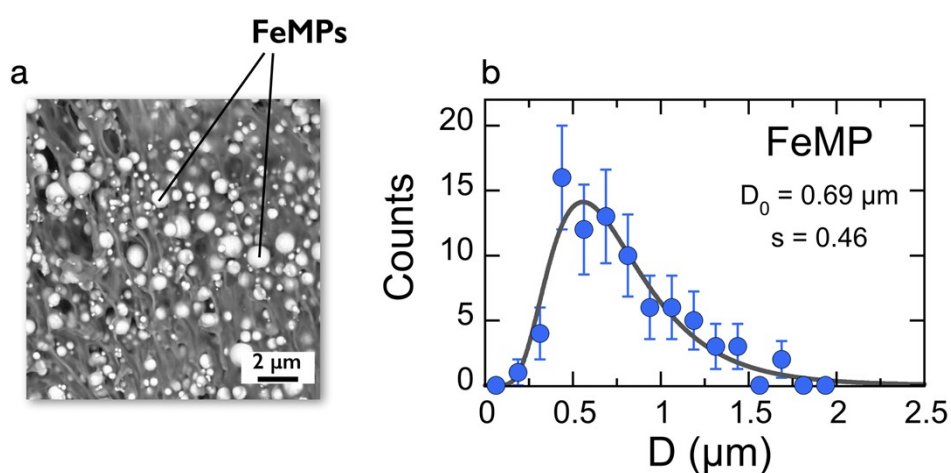


Figure S1: **a)** Transmission electron microscopy of iron carbonyl microparticles (FeMPs) embedded in a PDMS matrix. **b)** FeMP size distribution; the continuous line is the result of a best fit using a log-normal function with median diameter $D_0 = 0.69 \mu\text{m}$ and dispersity $s = 0.46$. The dispersity is defined as the ratio between the standard deviation and the average diameter.

Supporting Information S2

Elemental maps and fractions of carbon, silicon, iron and oxygen obtained from energy-dispersive X-ray (EDX) analysis

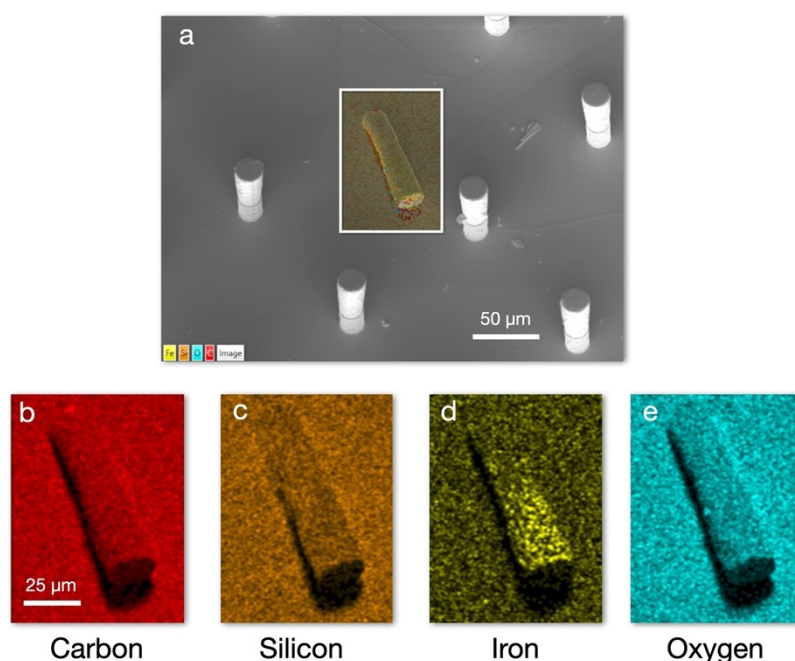


Figure S2-A: a) Superposition of scanning electron microscopy of magnetic pillars and EDX elemental maps of carbon, silicon, iron and oxygen. b-e) Individual mapping of the C, Si, Fe and O elements.

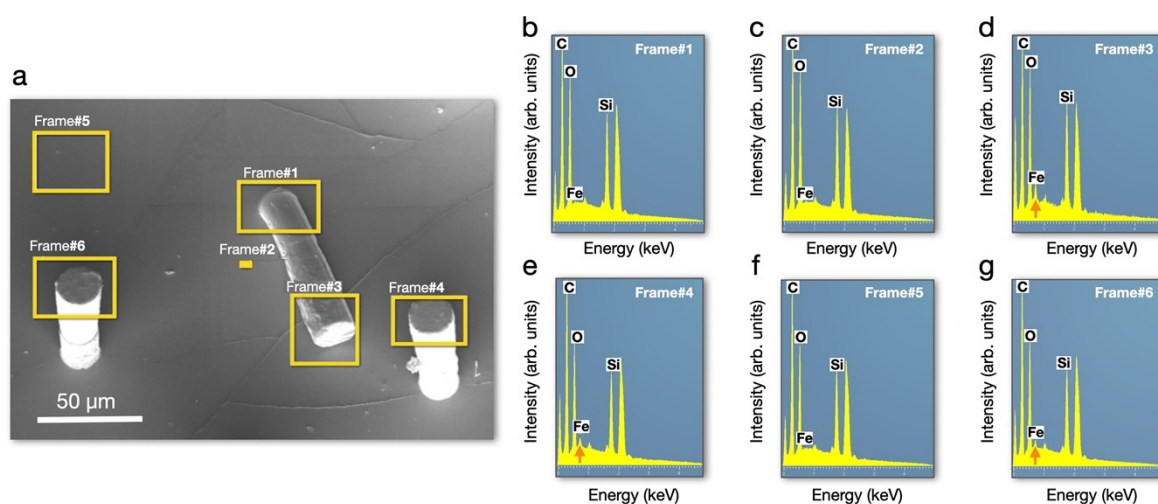


Figure S2-B: a) Scanning electron microscopy of pillar array. b-g) Associated EDX elemental proportions of carbon, oxygen, iron and silicon (Frame#1 to #6). The rectangles shown in a) denote the areas to which EDX has been applied. The orange arrows in d), e) and g) indicate the iron peak.

Label	Frame#1	Frame#2	Frame#3	Frame#4	Frame#6	Frame#6
C	32.84	32.51	28.13	34.11	36.04	34.26
O	24.81	24.74	22.05	21.40	22.76	21.73
Si	42.34	42.75	39.39	37.70	41.20	38.27
Fe	0.00	0.00	10.43	6.79	0.00	5.74
Total	100.00	100.00	100.00	100.00	100.00	100.00

Table S1: EDX elemental proportions of carbon, oxygen, iron and silicon obtained from a representative pillar array.

Supporting Information S3

Iron carbonyl microparticle (FeMPs) powder magnetization curve

The magnetization of iron microparticle powder (FeMP) was measured at room temperature ($T = 25\text{ }^\circ\text{C}$), using a frequency of 40 Hz. Cycles of magnetic excitation increasing from 0 to $1.59 \times 10^6\text{ A m}^{-1}$ and then decreasing back to 0 were performed at a scanning speed of $8 \times 10^3\text{ A m}^{-1}\text{ s}^{-1}$. **Fig. S3a** shows a iron carbonyl specimen and **Fig. 3b** shows the magnetization curve of FeMPs as a function of field strength.

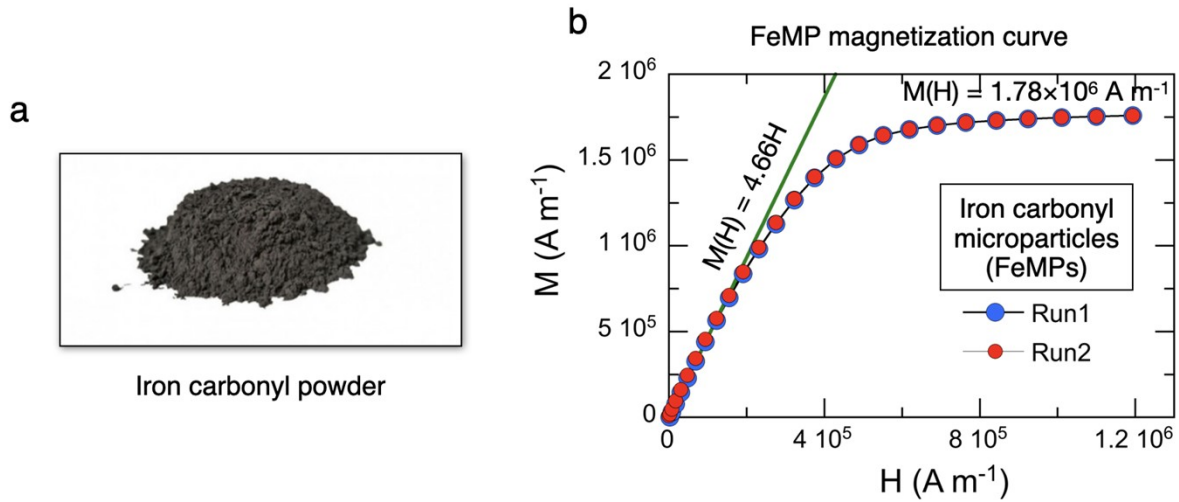


Figure S3: a) Iron carbonyl microparticles powder (FeMPs). b) Magnetization curve of FeMP powder as a function of applied magnetic excitation H . The fitting at low and high H -values makes it possible to determine the prefactor in the linear zone and the magnetization at saturation m_s .

High field regime, saturation

From the Langevin magnetization function, the high-field magnetization value ($\xi = \mu_0 m_s v H / k_B T \gg 1$) lead to:

$$M(H) = \phi m_s [\coth(\xi) - 1/\xi] = \phi m_s = 1.78 \times 10^6 \text{ A m}^{-1}$$

which reduces to ($\phi = 1$):

$$m_s = 1.78 \times 10^6 \text{ A m}^{-1}$$

In the previous equations, m_s is the magnetization at saturation, v the particle volume and $k_B T$ the thermal energy

This value is in good agreement with that obtained by B. Bolteau in 2018 ($1.72 \times 10^6 \text{ A m}^{-1}$) [1,2].

Low field regime, linear behavior

From the low-field magnetization, we have the expression:

$$M(H) = \phi m_s [\coth(\xi) - 1/\xi] \sim \frac{m_s \phi \xi(H)}{3} = \mu_0 \phi \frac{m_s^2 v}{3 k_B T} H$$

which reduces to ($\phi = 1$):

$$M(H) = \mu_0 \frac{m_s^2 v}{3 k_B T} H$$

Fitting the magnetization data to **Fig. S3b** gives: $M(H) = 4.66H$. Hence :

$$\mu_0 \frac{m_s^2 v}{3 k_B T} = 4.66$$

We deduce that the volume of the magnetic domains is $1.45 \times 10^{-26} \text{ m}^3$ and their diameter $d = 3.03 \text{ nm}$.

The saturation magnetization m_s , expressed in A m^{-1} or in emu g^{-1} is an important parameter of magnetic material. In **Table S2** are listed some m_s -values for the common iron oxide nanostructures.

Nanoparticles	Chemical formula	ρ kg m^{-3}	m_s A m^{-1}	m_s emu g^{-1}
Maghemite [3]	$\gamma\text{-Fe}_2\text{O}_3$	4900	3.5×10^5	72
Magnetite	Fe_3O_4	5170	4.4×10^5	86
FeMP [1,2]	Fe^0	7874	1.72×10^6	218
FeMP – this work	Fe^0	7874	1.78×10^6	226

Table S2: Mass density and saturation magnetization for common iron oxide nanostructures. The saturation magnetization expressed in A m^{-1} is obtained by multiplying the saturation magnetization expressed in emu g^{-1} by the mass density expressed in kg m^{-3} .

Supporting Information S4

Wide-Angle X-Ray Scattering (WAXS) on FeMP iron microparticles

X-ray scattering was carried out using an Empyrean (PANALYTICAL) diffractometer equipped with a multichannel PIXcel 3D detector and a Cobalt X-ray source (1.790307 Å). Samples were deposited on a monocrystalline Si substrate, with a spinner movement (rotation time 1 s). A 1/16° divergence slit, a 1/8° anti-scatter slit and a 10 mm mask were installed before the samples. Typically, each pattern was recorded in the $\theta - \theta$ Bragg-Brentano geometry in the 10°-20° 2θ range (0.0263° for 600 s), where 2θ denotes the scattering angle.

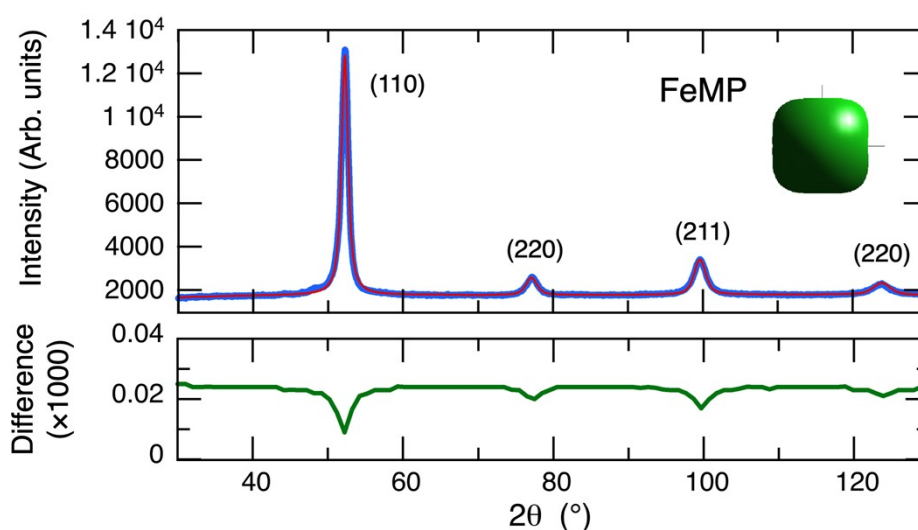


Figure S4: X-Ray diffractogram obtained on powder samples of iron microparticles (FeMP). The intensity shows 4 Bragg peaks (labeled (110), (220), (211) and (220)) associated with the body center cubic $Im\bar{3}m$ structure of an Fe^0 crystal. The lattice parameter derived from the peak position gives $a = 2.86776$ Å. From the widths of the peaks, the crystallite size was estimated at 9 ± 1 nm. The inset shows the crystallite shape that best matches the intensity data.

Supporting Information S5

Comparison of pillar motion along the x- and y-direction

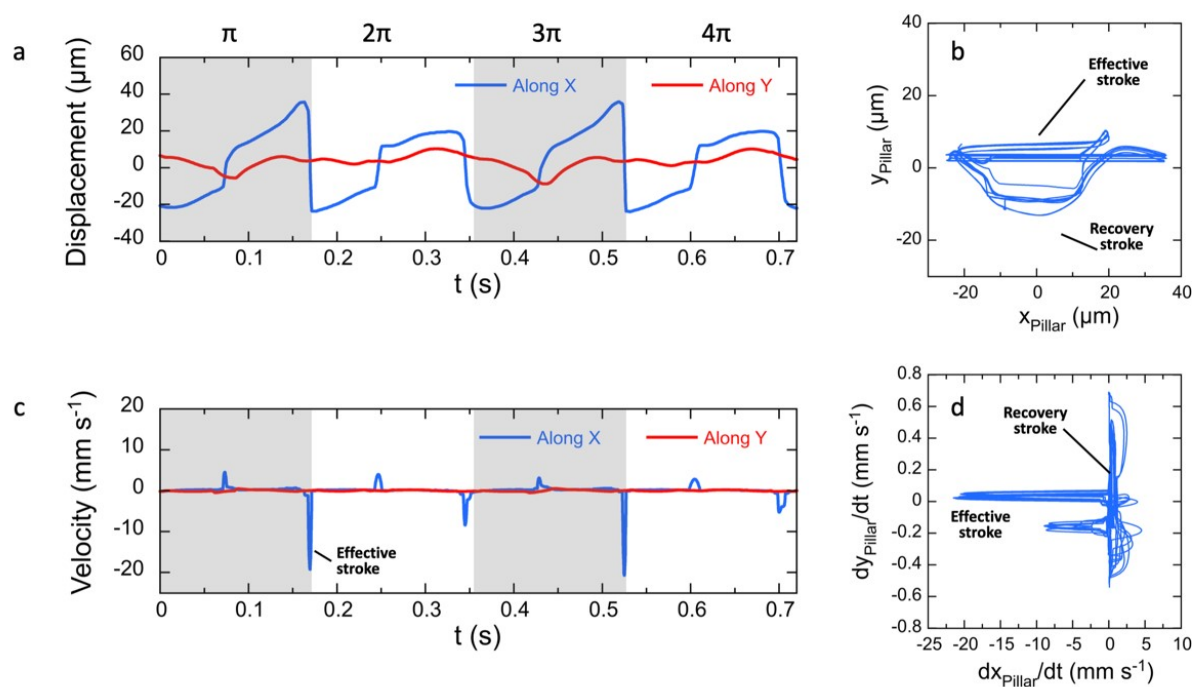


Figure S5: Pillar tip displacement and velocity profiles along the x - and y -directions corresponding to the data in Fig. 4. **a)** $x_{\text{Pillar}}(t)$ and $y_{\text{Pillar}}(t)$ as a function of time over two magnet rotation periods. **b)** $dx_{\text{Pillar}}(t)/dt$ and $dy_{\text{Pillar}}(t)/dt$ calculated from the data in Fig. S5a. **c)** Plot showing y_{Pillar} versus x_{Pillar} over 7 magnet rotation periods. **d)** Similar to Fig. S5c for the in velocities dy_{Pillar}/dt versus $dx_{\text{Pillar}}(t)/dt$. From the figure, it can be seen that the maximum velocity in the y -direction reaches approximately 3% of the corresponding value in the x -direction.

Supporting Information S6

Bead motion shows pulsatile pattern as a function of time

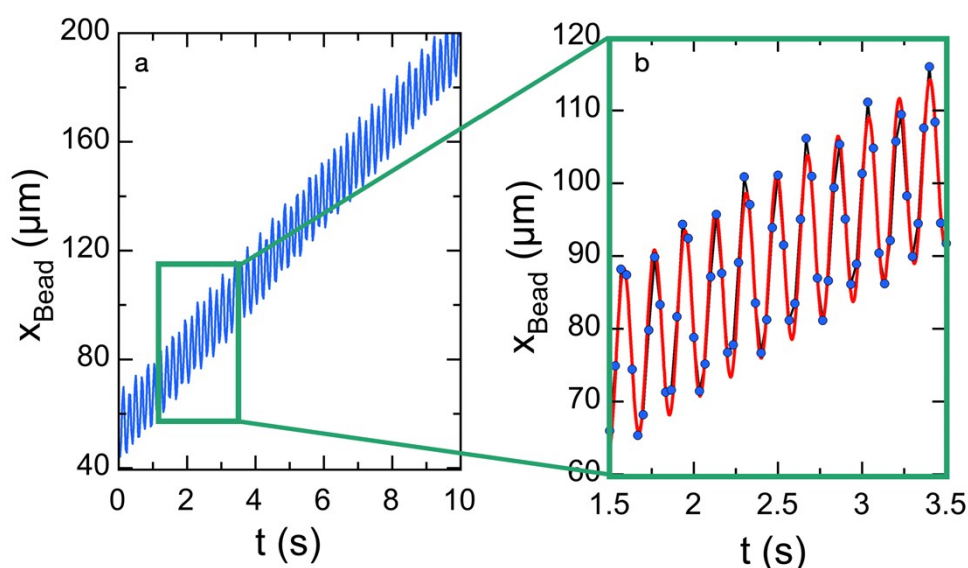


Figure S6: a) Image sequence using a high-speed camera (240 frames per second) shows that the movement of the beads along the x -axis is oscillatory, with an oscillation frequency corresponding to twice the magnet rotation frequency. The average speed obtained is positive and the particle is moving within the cell. **b)** A closer examination of the particle displacement caused by pillar beating reveals a pulsatile pattern, which can be approximated by the function: $x_{\text{Bead}}(t,z) = [dx_{\text{Bead}}(t,z)/dt]t + a(z)\sin(2\omega t)$. In the previous equation, $x_{\text{Bead}}(t,z)$ and $dx_{\text{Bead}}(t,z)/dt$ are the bead coordinate and velocity along the x -axis respectively, $a(z)$ a height-dependent constant and ω the magnet angular frequency. This function is shown in the figure as a solid red line. This oscillatory motion can be approximated by the linear term, yielding after averaging over 10-100 beads the velocity profile $V_x(z)$ (data from Fig. 5).

Supporting Information S7

Image of magnetic micropillar arrays in binocular microscopy

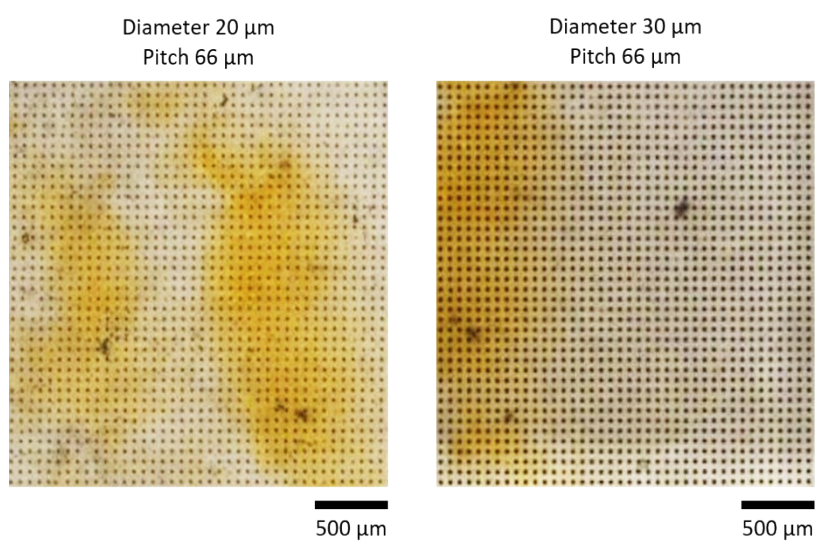


Figure S7: Binocular images of different pillar arrays with increasing diameters (20 and 30 µm). These data were used to count the number of pillars per microchip for the iron dosage assays (main text, **Fig. 1d**) [4,5].

Supporting Information S8

Magnetic field measurements under translational motion: experiments and simulations

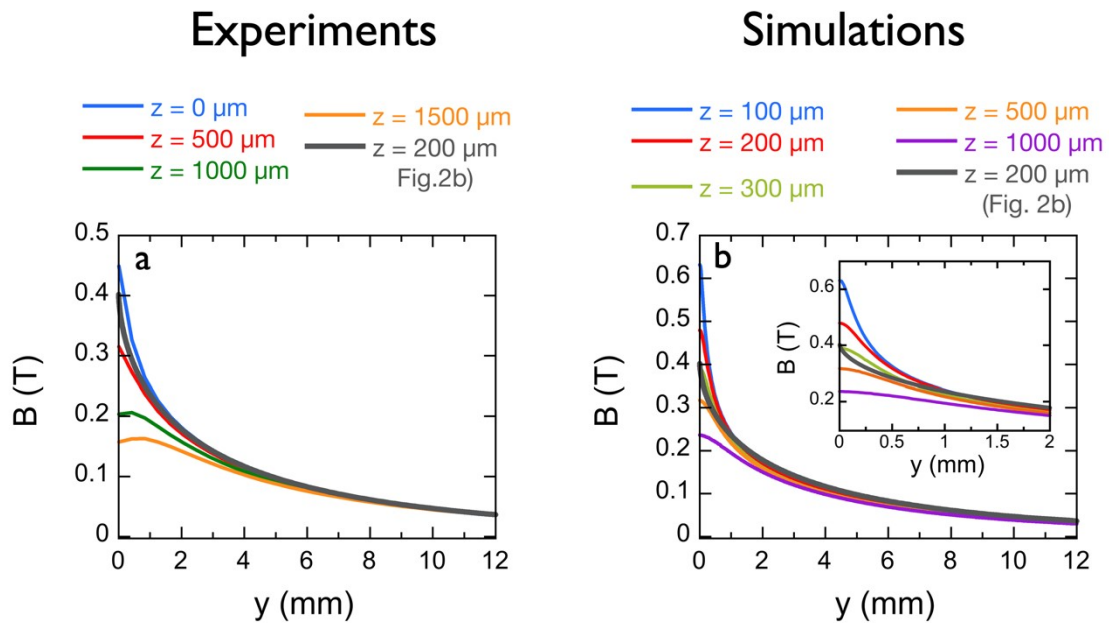


Figure S8: a) Variation of the magnetic field $B(y,z)$ as a function of the lateral position y , shown for several z -positions of the magnet. The dark grey curve corresponds to the experimental data presented in **Fig. 2b**. For $z = 0$ and $500 \mu\text{m}$, the magnetic field profiles are nearly identical, with noticeable deviations appearing at short distance, $y < 1 \text{ mm}$. **b)** $B(y,z)$ -data obtained from COMSOL finite element simulations. These results closely match the experimental profiles shown in **Fig. S8a**, particularly for $z = 200 - 300 \mu\text{m}$, consistent with the experimental data. **Inset:** Zoom of the region $y = 0 - 2 \text{ mm}$ for the simulation data.

Supporting Information S9

Detailed Simulation Procedure

The magnetic field of the magnetic pen is constructed in COMSOL Multiphysics 6.0 (COMSOL Inc. Stockholm Sweden) using the magnetic field - no currents module. A full description of the physics can be found in the COMSOL Reference manual [6]. In short, this module attempts to solve the magnetic flux conservation equations, such that:

$$-\nabla(\mu_0\nabla V_m - \mu_0 M_i) = 0 \quad (S9.1)$$

where V_m is the magnetic potential, μ_0 is the free space permeability, and M_i is the magnetization. These are in turn related to the magnetic field by:

$$B_i = \mu_0(H_{int,i} + M_i) \quad (S9.2)$$

And

$$H_{int,i} = -\nabla V_m \quad (S9.3)$$

where B_i is the magnetic flux density, and $H_{int,i}$ the internal magnetic field.

The geometry of the model is based off of that used experimentally for the magnetic pen and ciliated PDMS surface (For reference, see **Fig. 2a** in the main text). The magnets themselves are taken to have a length of $W = 11\text{mm}$, while the iron triangular prism measures the same $W_{mag} = 11\text{mm}$ on all sides. The geometry of the problem was cut along its central axis, as this represents the axis of symmetry for the magnetic pen, allowing us to reduce the computational cost by half. The magnets and iron prism therefore have an in-page depth of $W_{mag}/2 = 5.5\text{mm}$. A rectangular body representing the ciliated PDMS surface was also placed below the magnetic pen, such that the two make a 30° angle. Additionally, an aluminum wand measuring $d_{wand} = 6\text{mm}$ was attached to the back of the magnetic cubes. Overall, the simulation takes place in a $W_{air} = 20\text{mm}$ cube, with the tip of the magnetic pen at its center. It should also be noted that a small rectangular box was placed at the edge of the tip to allow for improved mesh refinement. The geometry was meshed using the software built in "extremely fine" automatic mesh refinement, with a single domain refinement near the magnetic pen tip, as shown in **Fig. S9-A**.

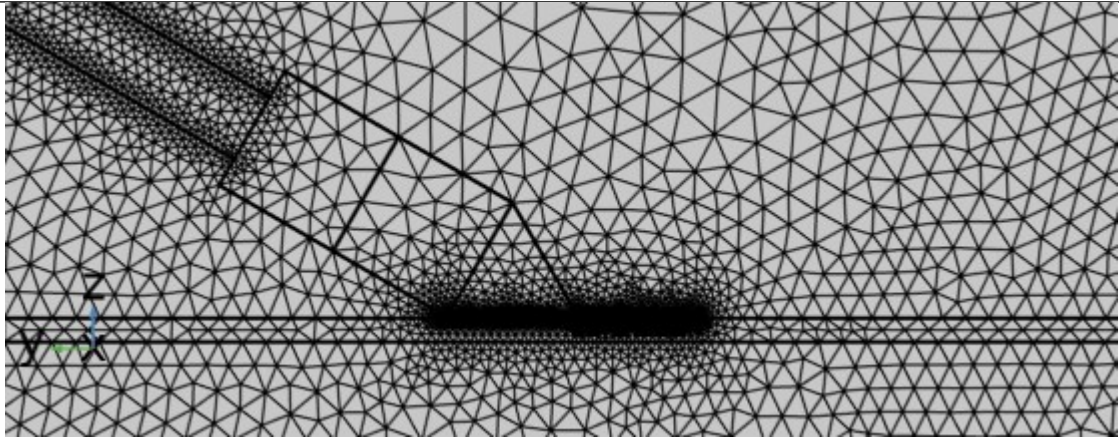


Figure S9-A: The automatic mesh generation of the simulated magnetic pen, with further refinement near the magnetic pen tip. The mesh is viewed along the axis of symmetry of the simulation.

All materials in the simulation used the built-in material properties from the COMSOL material library. The magnetic cubes were assigned as N42 neodymium magnets, with a remnant flux density of $B_{rem} = 1.3T$. This flux density was set to be in the direction of the magnetic tip, $\vec{e}_{mag} = (0, -1/2, -\sqrt{3}/2)$. The pen tip was set to be made of iron, with a relative permeability of $\mu_{r,Fe} = 4000$. The PDMS surface, aluminum wand, and surrounding air all had relative permeability of $\mu_r = 1$. The entire domain of the simulation was set to have magnetic flux conservation solved for in a steady state. The magnetic flux conservation was set to be solid for all materials, with properties taken from the material, except for the air domain, which was set to magnetic flux conservation fluid. The outer boundary of the simulation was set to be magnetically insulate, except the cut plane centered on the magnetic pen, which was set to the symmetry boundary condition. The volume of the bounding air box is assumed to be large enough to only negligibly affect the magnetic field near the magnetic pen tip. The simulation was a single step stationary simulation, with all settings left to the “physics-controlled” setting for default values. The stationary solver was given a relative tolerance of 0.001, with automatic linearity implemented, while the dependent variable solver scaling was left as “automatic”.

A separate simulation was prepared to model the bending of a magnetic micropillar. The micropillar was modeled using the COMSOL beam interface. The beam is anchored at its base, while the tip is left free, and magnetic forces and torques are applied to a fraction of the length of the beam. The beam itself is modeled using a standard circular geometry, with a diameter varying linearly from $d_b = 19 \mu\text{m}$ at its base, to $d_t = 21\mu\text{m}$ at its tip, with a total length of $l_{pillar} = 75 \mu\text{m}$. These values are supported by those previously measured by SEM (see main text **Fig. 1a&1c**). The elastic modulus and Poisson ratio for the beam was set to be uniform, estimating $E = 750 \text{ kPa}$ and $\nu = 0.35$ respectively as the default value. The simulation used an automatically generated mesh for the simulation, set to a very fine refinement. Standard COMSOL solver settings were used, with an error tolerance of 0.001.

The COMSOL beam simulation balances the forces acting upon a beam by solving the quasistatic Timoshenko beam equations, using the default options for a circular cross sectioned beam. In these equations, the force acting upon a beam, F_i is balanced by its resistance to bending by:

$$EI \frac{\partial^4 \delta_i}{\partial Z^4} = q_i - \frac{8I(1+\nu)}{\pi \kappa d^2} \frac{\partial^2 q_i}{\partial Z^2} \quad (S9.4)$$

where $q_i = \partial F_i / \partial Z$ is the distributed load, δ_i is the beam displacement, $I = \pi d^4 / 64$, and $\kappa = 0.9$. In this scenario, Z represents the direction along the length of the beam. A full description of these equations can be found in the COMSOL reference manual \cite{comsol_comsol_2019}. Furthermore, the moment along the length of the beam can be equated by:

$$\Gamma_i = -EI \frac{\partial \theta_{l,i}}{\partial Z} \quad (S9.5)$$

where $\theta_{l,i}$ is the bent angle of the beam perpendicular to the i direction. The fixed boundary condition at the pillar base ensures that both $\theta_{l,i} = 0$ and $\delta_i = 0$ at $Z = 0$.

The torque and Force applied to the beam used the exported magnetic field and gradients, B_i and $\frac{\partial B_i}{\partial x_j}$ exported from the magnetic field simulation (the field is shown in **Fig. 3a** of the main text). A free body diagram of the beam is shown in **Fig. S9-B**. The use of this field is based on the assumption that the micropillars are spaced sufficiently far apart so as to minimally affect the overall magnetic field between micropillars. The length of the beam over which this force and torque was applied, h_{FeMP} starting from its tip, was varied over several experiments. In order to simulate the effect of the approaching magnetic pen on the cilia, the magnetic field was set to vary with time. For a series of tests, the exported field B_i and $\frac{\partial B_i}{\partial x_j}$ at the position $(0, t, z_0)$ were taken, where t is the time step, equivalent to movement in the y direction, and z_0 was the z position along which tests were taken. All bending tests were performed along the axis of symmetry, $x = 0$.

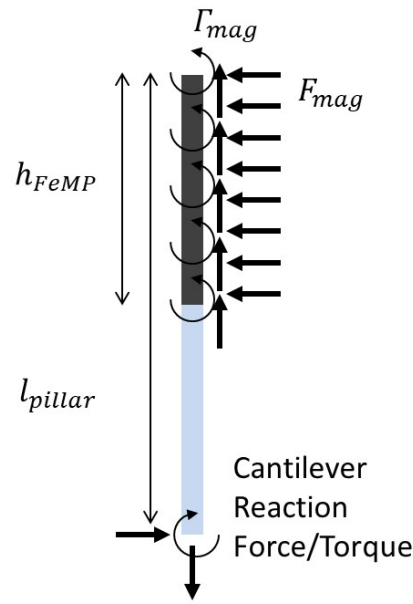


Figure S9-B: A free body diagram of the micropillar beam, including magnetic force and torque, as well as resultant forces at the immobile cantilever base.

The magnetic force per volume acting upon the top length of the beam is described as:

$$F_{mag,i} = \mu_0^{-1} \frac{M_j \partial B_i}{B \partial x_j} \quad (S9.6)$$

In this case, the magnetization is given by, $M = \phi_{FeMP} M_{FeMP}(B) / \phi_{\max(FeMP)}$, where $M_{FeMP}(B)$ is empirically measured magnetization curve measured by vibrating sample magnetometr (see **Fig. 1e**, main text). In order to account for the possibility of lower concentrations of FeMP within the micropillar, the magnetization is multiplied by the relative FeMP concentration, $\phi_{FeMP} / \phi_{\max(FeMP)}$ where ϕ_{FeMP} and ϕ_{pack} are the absolute concentration of iron within the micropillar, and the maximum concentration of iron in loose packed FeMP. Assuming the independent magnetization for each microparticle, **Eq. S9.6** is equivalent to:

$$F_{mag,i} = \frac{M_j \partial B_i}{\partial x_j} \quad (S9.7)$$

|

In addition to the applied force, a magnetic coupling torque was also applied to the beam length h_{FeMP} . This torque assumes interaction between the FeMPs, resulting in a geometric demagnetization. Approximating the micropillar as a simple cylinder, the demagnetization factors are approximated as $N_{ZZ} = 4l / (\sqrt{\pi}d + 1)$ and $2N_{YY} + N_{ZZ} = 1$ [7]. The demagnetization factors described above are only valid when aligned with the local axis of the micropillar. As such, the reference frame for each segment of the micropillar needed to be rotated relative to the micropillar bend angle.

As the applied external field in the absence of material is $B_i = \mu_0 H_{0,i}$, the magnetization and internal magnetic fields can be approximated by:

$$\frac{B}{\mu_0} \approx H_{int} + \phi_{FeMP} M(B) \quad (S9.8)$$

With this in mind, the magnetic moment per volume applied to the beam can be approximated by:

$$\Gamma_{mag} = \frac{\mu_0 B^2 M^2 (N_{YY} - N_{ZZ}) e_{B,i} e_{l,i} e_{B,i} e_{l,j} \epsilon_{i,j,k}}{(B + \mu_0 (N_{ZZ} - 1) M) (B + \mu_0 (N_{YY} - 1) M)} \quad (S9.9)$$

where $e_{B,i}$ and $e_{l,i}$ represent the directional unit vectors of the magnetic field and the beam respectively for each individual element of the beam.

Although the solution was time dependent, all physics were set to behave as quasistatic. This is in part to simplify calculations, and also reflects the slow approach of the magnetic pen to the micropillar array in the bending experiments performed here. The time dependent solver allowed for physics-controlled solutions for variables not solved for, while initial values used an initial expression solution, setting $\theta_{r,i} = 0$. This was possible as the simulation progressed from t

= -20 s (equivalent to $y = 20$ mm relative to the magnetic tip in terms of B_i and $\frac{\partial B_i}{\partial x_j}$), where $|B|$ is small, to directly below the magnet at $t =$ and $y = 0$. caling was set to “automatic” with a residual scaling of 1. A solution tolerance factor of 0.1 was set, with a relative tolerance of 0.001. A MUMP direct solver was used, as well as a direct linear solver with a tolerance factor of 1.

References

- [1] B. Bolteau, K. Dos Santos, F. Gelebart, J. Gomes, J. Teisseire, E. Barthel, J. Fresnais, New Platform for Gravitational Microfluidic Using Ferrofluids, *Langmuir* **35**, 9133-9138 (2019). doi: 10.1021/acs.langmuir.8b03423
- [2] B. Bolteau, F. Gelebart, J. Teisseire, E. Barthel, J. Fresnais, Digital Microfluidics—How Magnetically Driven Orientation of Pillars Influences Droplet Positioning, *ACS Appl. Mater. Interfaces* **15**, 35674-35683 (2023). doi: 10.1021/acsami.3c05734
- [3] J.-F. Berret, O. Sandre, A. Mauger, Size Distribution of Superparamagnetic Particles Determined by Magnetic Sedimentation, *Langmuir* **23**, 2993-2999 (2007). doi: 10.1021/la061958w
- [4] V. Torrisi, A. Graillet, L. Vitorazi, Q. Crouzet, G. Marletta, C. Loubat, J.-F. Berret, Preventing Corona Effects: Multiphosphonic Acid Poly(ethylene glycol) Copolymers for Stable Stealth Iron Oxide Nanoparticles, *Biomacromolecules* **15**, 3171-3179 (2014). doi: 10.1021/bm500832q
- [5] A. Galimard, M. Safi, N. Ould-Moussa, D. Montero, H. Conjeaud, J.F. Berret, Thirty-Femtogram Detection of Iron In Mammalian Cells, *Small* **8**, 2036-2044 (2012). doi: 10.1002/sml.201102356
- [6] COMSOL Multiphysics® v. 6.2. COMSOL AB, Stockholm, Sweden, 2019.

[7] M. Sato, Y. Ishii, Simple and Approximate Expressions of Demagnetizing Factors of Uniformly Magnetized Rectangular Rod and Cylinder, *J. Appl. Phys.* **66**, 983-985 (1989). doi: 10.1063/1.343481